Microstructure of Ni-Based Superalloy

Contributor: Łukasz Rakoczy, Bogdan Rutkowski

To understand the behaviour of the especially complex Ni-based superalloys at high-homologous temperatures it is necessary to characterize their microstructure in fully heat-treatment condition. Detection and characterization of precipitates even nano-precipitates is essential in the study of creep and fatigue degradation. Without the knowledge about the phase composition of material, it is problematic to predict the microstructure evolution during long-term service. The main aim of this work was to perform the comprehensive characterization of equiaxed Ni-based superalloy René 108 from micro- to atomic-scale resolution by using analytical microscopy techniques.

1. Introduction

Ni-based alloys used for working at high homologous temperatures are the most advanced metallic construction materials. The unique combination of high strength and excellent oxidation resistance makes it an irreplaceable group of materials in aerospace, power and nuclear industries. The usefulness of Ni-based superalloys during long-term service at harsh conditions depends strongly on the alloying elements, their concentrations and the morphology of the main strengthening phases [1][2][3][4]. The development of the first Ni-based superalloys began over 100 years ago. It happened around 1918 with the patenting of the Ni-20Cr alloy (Nichrome) [5][6]. It became a progenitor for the next superalloys of the Nimonic and Inconel series [7]. In 1929 Bedford, Pilling and Merica presented the results of the study on the influence of Al and Ti on the mechanical properties of the Nichrome superalloy [1][5]. They noticed that the addition of these elements significantly increases creep resistance. Despite difficulties in observing fine precipitates responsible for the strengthening, several subsequent Ni-based superalloys were developed [8]. In the following years, some of the nickel content was replaced with cobalt, thus increasing the high-temperature oxidation resistance. One of the main representatives of Ni-Cr-Co alloys was Nimonic 90 with 20% of cobalt [9]. In 30's the gas turbine design by Elling had an operating temperature which did not exceed 550 ˚C [10]. There was no huge demand for Ni-based superalloys because the austenitic stainless steels could still work safely at this temperature. Several years later engines constructed by Heinkel and Whittle led to breakthrough in the Ni-superalloys' development because the service temperature reached 780 ˚C [11][12]. Conventional stainless steels were not able to meet the growing requirements [13]. During the Second World War superalloys were therefore modified by introducing even higher amounts of aluminium and titanium. Meanwhile, at the end of the 1940s, it was noticed that the additions of refractory elements, like Mo, contribute to a significant solution and precipitation strengthening with carbides. In the 1940s, engine components were manufactured by forging and air casting and so the strength and metallurgical purity were not the highest. Introduction of vacuum casting technology in 1952 was considered to be the most essential step towards improving the mechanical properties and purity of both cast and wrought superalloys [4][14]. Before the advent of vacuum melting and casting techniques, cast superalloys did not gain wide acceptance for a turbine blade application. One of the first alloys to be vacuum cast was Inconel 713C and this became widely used in the aerospace industry. The high carbon content contributed to excessive primary carbides, poor ductility at low temperatures and problems with integrally bladed disc castings. To overcome this issue, a low carbon version of the alloy was made and is also widely used for turbine blades [14][15][16]. In the late 1950s, H.L. Eiselstein developed Inconel 718 precipitation strengthened by intermetallic phase γ'' (Ni_3Nb), which, along with the Waspaloy, was quickly put into continuous production [4][17]. In the 60s, it began to be seen that chromium could be partially replaced to achieve even higher creep resistance. However, limiting its concentration sensitized superalloys to high-temperature corrosion and so more attention was paid to its influence on microstructure and properties[4][18]. Numerous chemical composition modifications broadened the knowledge of metallurgists and allowed to develop new grades of superalloys, but also this was associated with design faults. Excessive amounts of alloying elements led to the formation of detrimental topologically closed phases (TCP) [19]. These undesired results indicated that in such complex materials design, it is necessary to use additional tools, computer software [20]. In the late 1960s, the strengthening of superalloys by only increasing Al and Ti became impractical. Taking into account only weight fraction, they were not the dominant alloying elements. Their too high concentration prevents the production of complex castings due to brittleness and so Al+Ti

concentration usually does not exceed 8% [21][22]. Thanks to lowering of the Ti concentration, the castability was considerably improved, which consequently led to design of the new superalloys with low Ti/Al ratio [23]. Additionally the Mo and Ta concentrations were increased in order to strengthen the γ-matrix. The proposal of molybdenum replacement by tungsten was adopted during the development of the MAR M200 by Martin Metals Company. Too high creep rate led to premature failure, and in response to this result, the superalloy was modified by hafnium, and so the MAR M002 introduced [14][24]. Hf leads to fine and stable MC carbides' formation. This contributed to the modification of many previously developed superalloys like Inconel 713C (to MM-004) and B1900 (to MM-007) [25][26]. Another, approach to overcoming the intermediate temperature ductility problem in cast superalloys has been the development of the so-called BC superalloys [14][27]. Maxwell [28] found that the high boron content (0.1-0.16%) with a low carbon concentration guarantees the improvement of the creep resistance of MAR M200 superalloy at 760 ˚C, without reducing other properties. Quichou [29] confirmed that BC superalloys were characterized by better castability properties than IN792, IN792+Hf and IN100. This impact was the result of borides formation in the grain boundaries. A similar effect was obtained in many other superalloys, thanks to which boron is still an essential alloying element [30][31][32]. In the following years, the design of polycrystalline alloys assumed the use of all previously known mechanisms. After several decades the archetype of the superalloys, two-component Nichrome, was modified to such an extent that the alloying elements exceeded twelve. The best examples of which are the microstructurally complex superalloys as MAR-M247 and Inconel 792+Hf [33][34][35].

2. Microstructure of René 108 Superalloy by LM and SEM

The unetched microstructure of the superalloy reveals the carbides' distribution and their morphology (Figure 1a). Their volume fraction is 0.88% (±0.16%). The high standard deviation resulted from their uneven distribution in the casting volume. Carbides are characterized by a complex morphology, namely small regular blocks, elongated parallelograms with smooth edges, and "chinese script". The last one usually consisted of three separate parts: the central core terminated with an angular head and perpendicularly arranged elongated arms. The core and arms were made of fine, irregular carbides, not like thick plates and rods. Etching revealed the dendritic structure of the casting and significant local microsegregation of microstructural components (Figure 1b). Despite the heat treatment (solution + ageing), the microstructure is still very heterogeneous. The high content of alloying elements, with their limited solubility in the γ matrix, has led to the formation of numerous constituents. The dendritic areas are characterized by a relatively homogeneous microstructure with γ' precipitates of various sizes. In the interdendritic spaces, carbides and eutectic islands γ-γ' are additionally present.
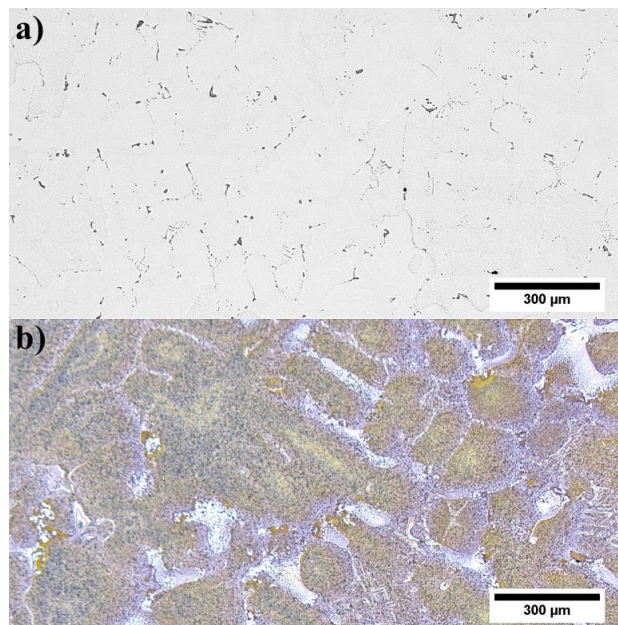

Figure 1. Microstructure of René 108: a) unetched; b) etched, LM

Significant differences in the microstructure of dendritic areas in relation to interdendritic spaces indicate that segregation of the alloying elements is present. To show this quantitatively, SEM-EDX measurements in these both regions were carried out. The data were used to calculate the segregation coefficient k^i of each alloying element. The ratio of the concentration of an alloying element in the centerline of dendrite arms to the concentration in the interdendritic spaces was calculated and is presented in Figure 2. Results confirm the irregular distribution of elements. The ki values, when lower than one, indicate that the element segregates to interdendritic spaces. When $k^i > 1$, the element is more

concentrated in the dendritic regions. Elements that strongly segregate to interdendritic spaces are Hf, Ta, Ti, and Al. When k^i values are below one, corresponding to W, Co, and Cr, these elements are more concentrated in dendrites. The most uniform distribution is observed for Ni and Mo.
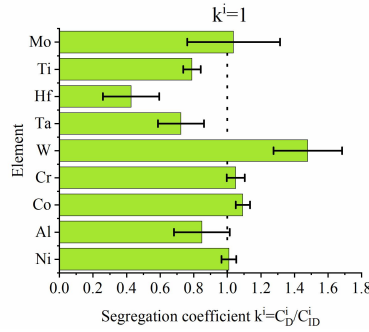

Figure 2. Segregation coefficient of selected alloying elements

Using a backscattered detector, SEM images with a strong dependence on the average atomic number Z were obtained. The microstructure of the γ' in dendritic regions is presented in Figure 3. Large secondary γ' precipitates are characterised by a complex morphology. Locally at their edges, there are single precipitates. During homogenization, secondary γ' precipitates were dissolving in the matrix. Some of those that were not completely dissolved, coagulated and coalesced. During cooling, they became nucleation sites for re-precipitating from the supersaturated γ solution. The misfit stresses between the γ and γ' phases promoted nucleation in the stress field of subsequent precipitates in these sites. Finer secondary γ' precipitates had a cubic-like morphology. The differences in their morphology are due to the various temperatures and time ranges in which they formed, as well as the low coagulation rate during ageing. Inside the γ channels, between secondary γ' precipitates, spherical tertiary γ' precipitates are revealed, formed independently from the supersaturated matrix during cooling after the ageing treatment. The volume fraction of the γ' precipitates within the dendrites calculated using SEM-BSE images is 54.99% (±3.65%). The γ' mean radius distribution presented in Figure 4a clearly reveals three classes which belong to large and fine secondary γ' and also tertiary γ'. Based on the area and perimeter of each precipitate, its shape coefficient was calculated. All obtained values are summarised in Figure 4b. Two curves are fitted to the distribution. The green one corresponds to the large secondary γ' precipitates and the second pink with cubic secondary and spherical tertiary γ'. According to the shape factor equation $\xi = (4\Pi * Area)/(Perimeter^2)$, the cubic precipitates have a coefficient of $\zeta=0.785$, while the spherical ζ of 1.0. Variation in nature (size, shape, and volume fraction) of γ′ precipitates is observed among others due to the effects of microsegregation and local cooling rates during casting solidification.
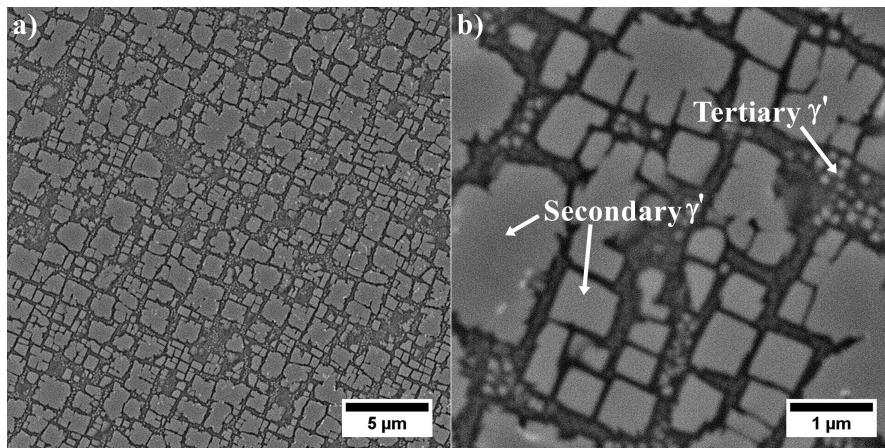

Figure 3. Microstructure of precipitates in dendrite arm: a) secondary γ'; b) secondary and fine tertiary γ'
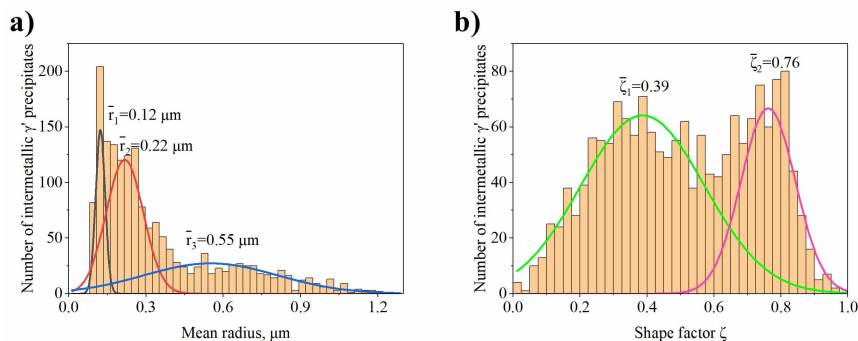

Figure 4. a) the mean γ' radius distribution; b) shape coefficient ζ distribution

In the interdendritic spaces, the primary, secondary, and tertiary γ' precipitates are characterized by much greater variability in distribution and morphology (Figure 5). These factors do not allow us to compare effectively stereological parameters with precipitates inside the dendrites. Especially complex morphology have primary γ' precipitates created at the end of casting's solidification through L→γ+γ' phase transformation. It is suggested that phase transformation was monovariant, namely progressing in the temperature range. The dissolution of large eutectics is challenging during industrial solid solution treatment, while increasing the solution temperature may lead to undesirable incipient melting. The eutectic γ-γ' islands are an unwanted component in superalloys, but its complete dissolution in the matrix during solution treatment is not possible. However, the high solution temperature changed the thermodynamic conditions and lead to partial dissolution, which consequently influenced the differentiation of the size of the secondary precipitates of the γ' phase around the eutectic γ-γ' islands.
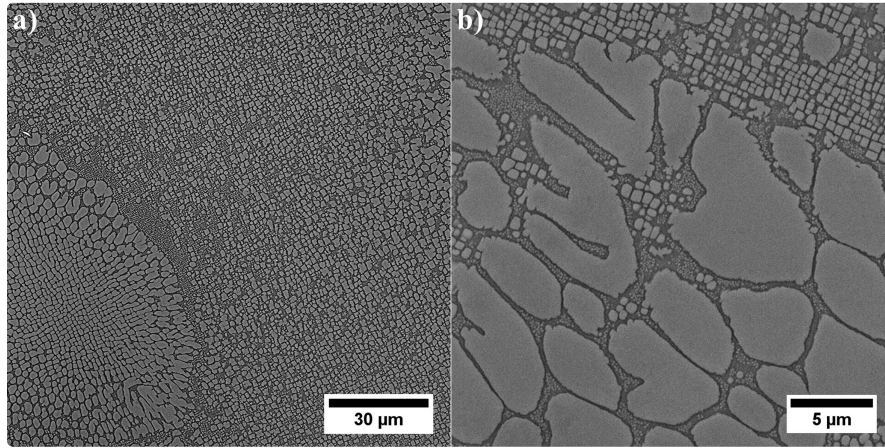

Figure 5. Microstructure of γ' precipitates in interdendritic space: a) difference in size and morphology of precipitates; b) large primary γ' precipitates

MC precipitates, appear as "white" precipitates and are concentrated in the interdendritic areas. For all of them, the Z-contrast is almost the same. Semi-quantitative SEM-EDX analyses of MC carbides were carried out to show the relationships between carbide formers, because it is widely known that carbides of metals belonging to the same class show considerable inter-solubility. Results from selected locations are presented in Figure 6 and Table 1. In chemical compositions of all carbides, strong carbide formers dominate, especially hafnium and tantalum. The mutual relation between these elements changes, depending on the shape and size of a precipitate. The following relationships were calculated between the elements with the highest affinity for carbon: Ta/Hf, (Ta+Hf/(W+Ti) and (Ta/Hf)/(W+Ti). Blocky shaped carbides with sharp edges located in the close vicinity of eutectic γ-γ' islands are the only ones characterized by a low Ta/Hf ratio and a very high (Ta+Hf)/(W+Ti) (more than a dozen). The carbides surrounded by the coarse γ' phase had the Ta/Hf and (Ta+Hf)/(W+Ti) coefficients in the range 2.0-3.0 and the (Ta/Hf)/(W+Ti)≤0.1. The morphology of the last group of carbides is similar to previously described, with one general difference, lack of surrounding coarse γ'. Relation Ta/Hf is 0.29-0.75, whereas (Ta+Hf)/(W+Ti) is in the range 4.75-8.06 and the (Ta/Hf)/(W+Ti)≤0.05. Additional 40 measurements were performed to present graphically the concentration relationships between strong carbide formers in the carbides' composition (Figure 7). Relationships in the corners of the graph correspond with these in Table 1.
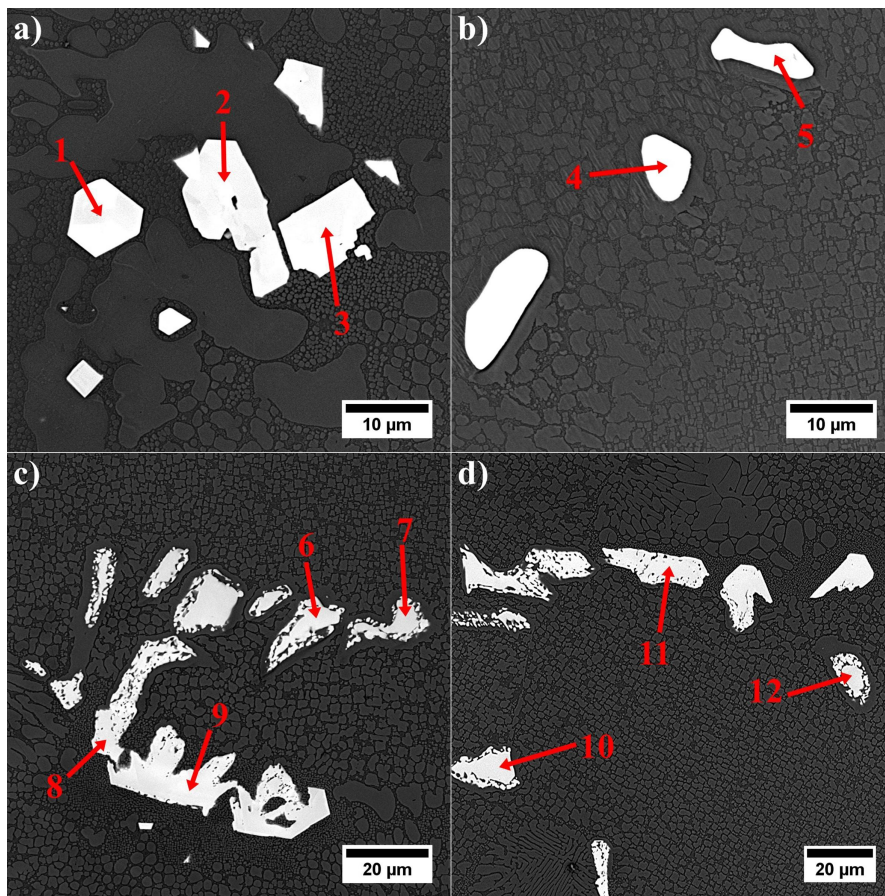
Figure 6. Microstructure of MC carbides and location of SEM-EDX analysis points: a) blocky carbides and points no. 1-3; b-c) carbides surrounded by the coarse γ' and points no. 4-9; d) morphologically complex carbides and points no. 10-12

Table 1. Results of SEM-EDX analysis in MC carbides, at%

No.	Ta	Hf	Ti	Ni	W	Co	Cr	Mo	Ta/Hf	(Ta+Hf)/(W+Ti)	(Ta/Hf)/(W+Ti)
1	12.2	75.0	1.1	6.9	1.0	1.4	1.0	1.4	0.16	42.95	0.08
2	16.3	73.3	1.2	5.4	1.2	1.0	0.9	0.7	0.22	37.99	0.09
3	16.6	72.3	2.0	6.0	0.8	0.7	1.1	0.5	0.23	32.32	0.08
4	42.5	21.1	17.4	7.7	5.9	2.4	1.8	1.3	2.01	2.73	0.09
5	42.7	16.8	19.1	8.2	7.1	2.4	2.3	1.4	2.54	2.27	0.10
6	43.9	19.9	19.5	6.9	5.5	0.9	1.6	1.8	2.20	2.56	0.09
7	42.8	18.3	18.4	7.9	7.0	2.2	1.8	1.7	2.35	2.40	0.09
8	23.4	54.5	6.5	5.7	5.9	1.4	1.0	1.6	0.43	6.26	0.03
9	17.5	61.1	4.2	5.9	5.5	2.9	2.1	1.0	0.29	8.06	0.03
10	44.9	21.5	18.9	5.9	5.2	1.1	1.0	1.5	2.09	2.76	0.09
11	30.9	41.3	10.0	6.9	5.2	2.6	2.0	1.1	0.75	4.75	0.05

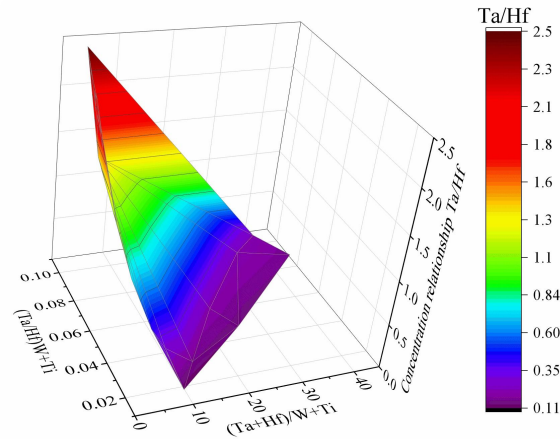| 12 | 20.2 | 19.9 | 6.4 | 5.6 | 1.1 | 1.9 | 1.6 | 20.2 | 2.15 | 2.49 | 0.08 |

Figure 7. Graphical representation of selected concentration relationships between alloying elements in carbides. Based on the SEM-EDX point analysis

At a grain boundary, continuous or semi-continuous layers of fine precipitates with irregular morphology are observed (Figure 8a-b). Crosswise to the grain boundary, a linear analysis of the distribution of selected alloying elements in one of these precipitates was performed (Figure 8c-d). Enrichment in chromium and tungsten is revealed, and also slightly increased Mo content. Alloying elements like Cr, W and Mo are generally known to have a high affinity for boron/carbon, and the solid solubility of boron/carbon in the γ phase is very low. It is likely that borides and/or secondary carbides can easily form at the grain boundaries in René 108.
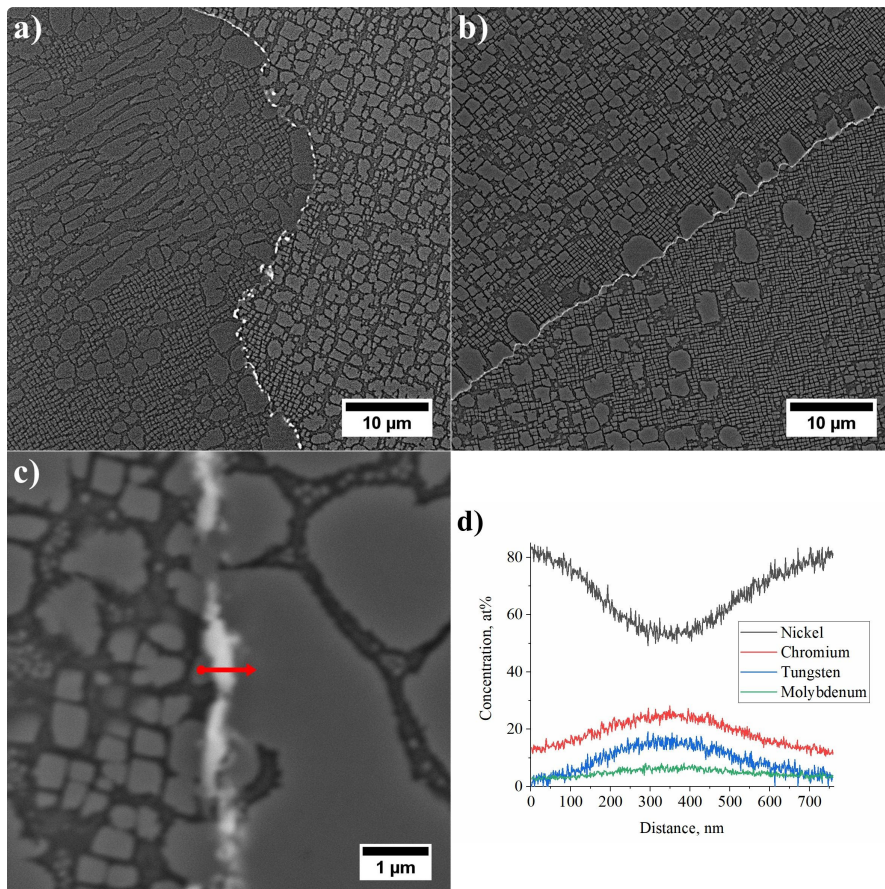

Figure 8. a-b) microstructure of precipitates at the grain boundaries; c) location of linear SEM-EDX analysis; d) distribution of selected alloying elements at a grain boundary

3. Characterization of strengthening phases by STEM and HRSTEM

3.1. Dendritic regions

The γ phase constituting the matrix of René 108 superalloy is strengthened mainly with the γ' phase. In the narrow channels of the γ matrix, between the large secondary γ' precipitates, nanometric tertiary γ' precipitates are present (Figure 9). The interfaces γ/γ' are additionally occupied by bright nano-precipitates. The degree of strengthening and mechanical properties depend on the chemical composition of the precipitates and the matrix, as well as the mutual crystallographic relationship which was also analysed.
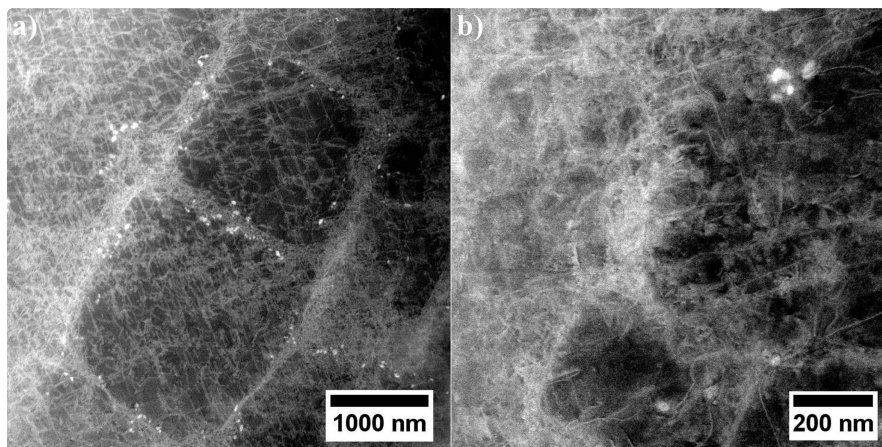

Figure 9. Microstructure of secondary γ' with nano-precipitates at the γ/γ' interface: a) cubic-shaped γ' precipitates; b) complex-shaped γ' precipitate, STEM-HAADF

The STEM-HAADF microstructure of dendritic region contains nano-precipitates at the interfaces γ/γ'. Bright contrast indicates that they consist mainly of elements with higher atomic numbers Z than those in phases γ and γ' (Figure 9a). During observations of thin foils at higher magnification, it was confirmed that these precipitates differ in morphology (Figure 10), with the first precipitate type being polygon-shaped with a 50 nm diameter, and the second type being diamond-shaped (50 x 25 nm).
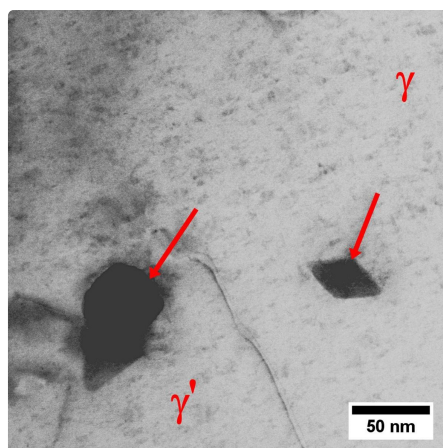

Figure 10. Nano-precipitates in dendritic regions, STEM-BF

Nanostructure of the precipitates and their interfaces with the γ' is shown in Figure 11. Based on the FFT image analysis, both precipitates are confirmed to be M_5B_3 borides. This phase is characterized by a body-centered tetragonal crystal structure with the space group I4/mcm and lattice parameters of a=5.46 Å and c=10.64 Å[36]. It has a $D8_1$-type structure (Strukturbericht notation) based on the information of atomic occupations in M_5B_3 phase. The atomic structure of boride obtained along the four-fold $[001]M_5B_3$ direction of the M_5B_3 phase is presented in Figure 11b. Although B atoms are invisible in the HAADF images due to their weak scattering ability, the structural characteristics of the M_5B_3 phase can be displayed. Imaging M_5B_3 along [001] zone axis reveals only one type of Wyckoff site.

Figure 11. Nanostructure of the M₅B₃ boride with corresponding FFT image: a) Zone axis [3-10] M₅B₃; b) Zone axis [001]M₅B₃, HRSTEM-HAADF

The STEM-EDX mapping of alloying elements covering the γ matrix channel and γ' precipitates with nano-precipitates at the γ/γ' interface is presented in Figure 12. Additionally, the quantitative analysis was carried out in 5 regions (Table 2). It was found that the main elements strengthening the γ matrix (precipitates-free zone, PFZ) are Cr and Co, with concentrations of over 35 at%. Among the elements which usually form (with Ni) the γ' precipitates are Al, Ti, Ta and Hf. Their total concentration in the secondary γ' phase is 17 at%, while in the tertiary is slightly lower, 15.4 at%.

Figure 12. Distribution of selected alloying elements in a dendritic region, STEM-EDX

Table 2. Chemical composition of the precipitates in dendritic regions, STEM-EDX, at%

Area	Phase	Ni	Cr	Co	W	Al	Ta	Hf	Ti	Mo

1	Matrix γ	52.1	21.5	16.9	4.7	3.4	0.3	0.2	0.2	0.7
2	Secondary γ'	69.8	2.9	6.8	3.2	13.7	1.6	0.6	1.1	0.3
3	Tertiary γ'	69.4	2.8	7.3	4.8	13.4	0.9	0.3	0.8	0.5
4	Boride M_5B_3	10.0	35.5	3.2	42.0	2.3	1.2	0.3	0.4	5.2
5		50.9	12.4	5.9	17.1	9.4	1.3	0.4	0.7	1.9

The mapping and analysis in selected areas confirmed that the partitioning of the alloying elements occurs between γ and γ' phases. The additional chemical composition measurements by STEM-EDX of γ matrix and secondary γ' phases were performed in 10 other locations to obtain better statistics; the results are presented in Figure 13. The elements most strongly segregating to the intermetallic γ' precipitates, i.e. those placed in the first quarter, are Ni, Al, Ta, Ti and Hf. Alloying elements in the γ' phase alter the formation energies of anti-phase boundaries (APBs), super lattice intrinsic stacking faults (SISFs), and complex stacking faults (CSFs), and may also directly influence the strength and plasticity of the γ' phase. The strengthening effect of the intermetallic γ' precipitates could be improved by the presence of elements like Ta and Ti because that Ta-Ta and Ti-Ti bonds have higher energies than Al-Al bond [37].
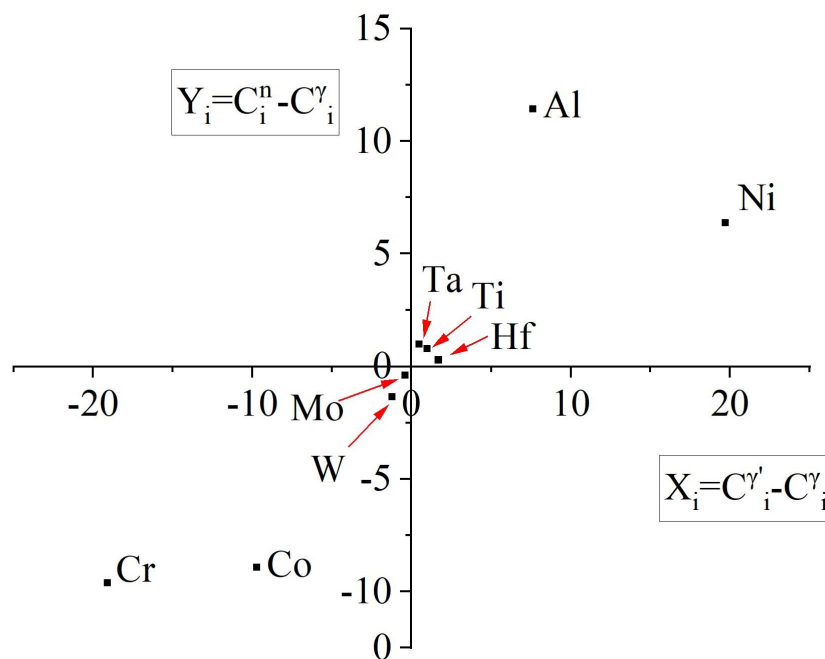

Figure 13. Concentration relationships between the bulk superalloy, secondary γ' and matrix

In accord with results of STEM-EDX analyses, in areas no. 4 and 5 (Table 2) borides are enriched in W, Cr, and Mo. Therefore they can be described by the formula $(W, Cr, Mo)_5B_3$. The concentration relationship of the two dominant W/Cr elements in the examined areas is 1.2, and 1.4, respectively, and the W/Mo relationship is 8.1 and 9.0. These

relations are therefore very similar, and the differences in the relative concentration results from the small thickness of the precipitate with a diamond shape. The distribution of selected elements presented in Figure 14 shows the sharp increase of tungsten concentration at the interface γ/M_5B_3. In the case of Cr, the concentration growth is more smoother and occurs for a longer distance.
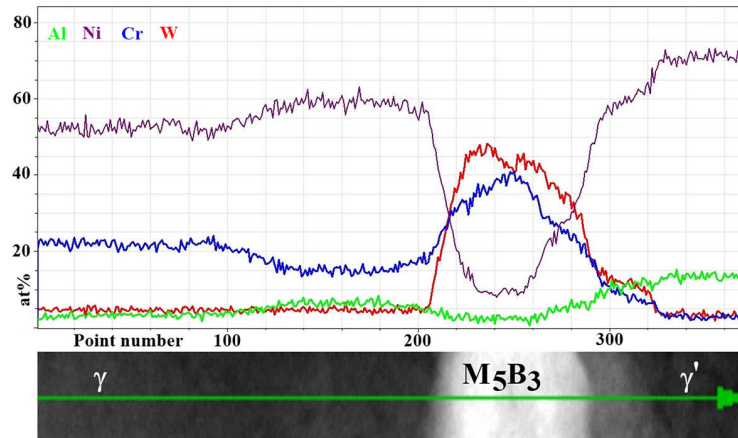

Figure 14. Distribution of selected alloying elements in γ, M_5B_3 and γ' phases, STEM-EDX

3.2. Interdendritic spaces

Numerous Hf and Ta-rich carbides, as well as the γ-γ' eutectic islands, were revealed during the SEM studies in interdendritic spaces. Further observations with transmission electron microscopy were done to show the remaining phases. The microstructure of the interdendritic spaces is much more complex than that of the dendritic regions. The difference is due both to the more complex morphology of the precipitates and their phase contrast. One similarity to the dendritic regions is numerous M_5B_3 borides at the γ/γ' interfaces (Figure 15). It should be noted that boron may reduce the solubility of carbon in the γ matrix, which promotes carbides' precipitation.
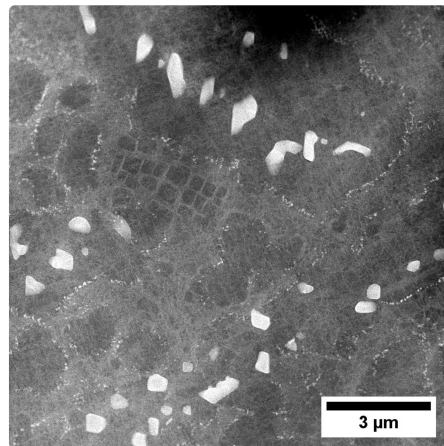

Figure 15. Microstructure of precipitates in the interdenritic spaces, STEM-HAADF

The chemical composition of primary and secondary (cubic) γ' was investigated. The locations of mapping, distribution of selected alloying elements, and the areas subjected to quantitative analysis are shown in Figure 16 and Table 3. In areas no. 1 and 2 involving primary γ' precipitates, the total content of γ'-formers (Al, Ti, Ta, Hf) is 15.5 at% and 16.1 at%, respectively. In the areas no. 3-4, which correspond to the secondary γ' precipitates, the values are lower and ranged from 13.3-14.9 at%.
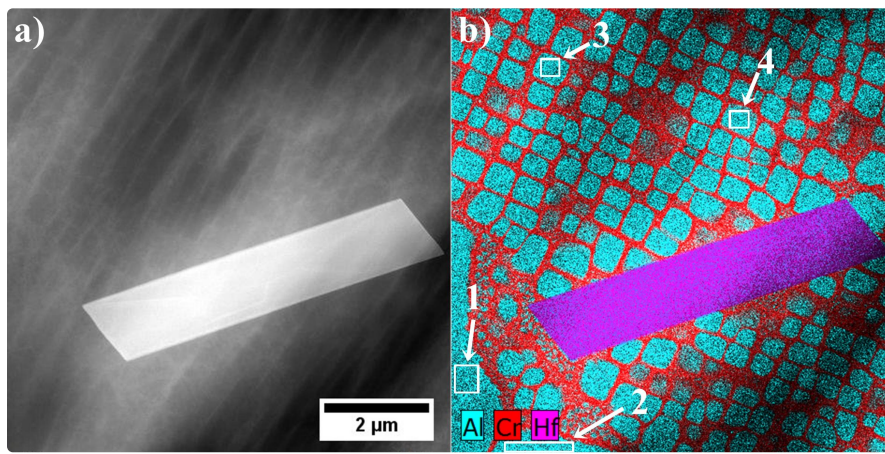
Figure 16. a) location of mapping; b) distribution of selected alloying elements in the area of primary γ', secondary γ', and MC carbide, STEM-EDX

Table 3. Chemical composition of the primary and secondary γ' precipitates in interdendritic space, STEM-EDX, at%

Area	Phase	Ni	Cr	Co	W	Al	Ta	Hf	Ti	Mo
1		71.0	3.5	7.1	2.6	11.6	1.4	1.1	1.4	0.3
	Primary γ'									
2		70.2	3.6	7.0	2.8	12.3	1.5	1.0	1.3	0.3
3		71.8	2.7	6.5	2.7	11.2	1.3	1.0	1.4	0.6
	Secondary γ'									
4		74.1	2.7	6.5	3.1	10.0	1.3	0.9	1.1	0.5

STEM-EDX mapping was performed in the region which includes a fragment of the "chinese script" carbide, surrounded by a coarse γ' precipitate (Figures 17 and 18). Additionally, three quantitative analyses of the coarse γ' chemical composition were carried out. Based on the results in Table 4, the total content of Al, Ta, Ti and Hf in the γ' phase precipitates in an area no. 1-3 is 17.3 at%, 16.3 at%, and 16.9 at%, respectively. The Cr distribution revealed the nano-precipitates that were not observed by SEM. They are present locally on the edges of the MC carbides and are composed of mainly of Cr, whose concentration is clearly higher than of W and Mo. Thus, the Cr/W relation in region no. 4 and 5 is 21.9 and 13.3, respectively. It should be noted that similar layers enriched in Cr were not found on the edge of blocky carbides near eutectic γ-γ' islands, which indicates differences in thermodynamical stability at elevated temperatures.
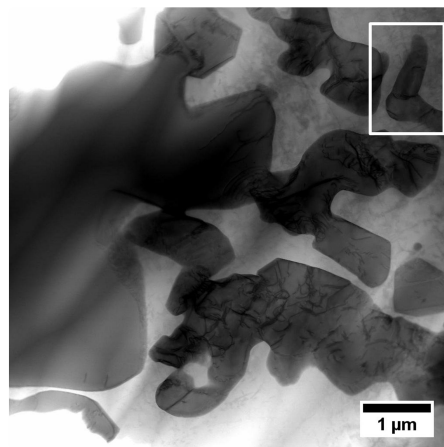

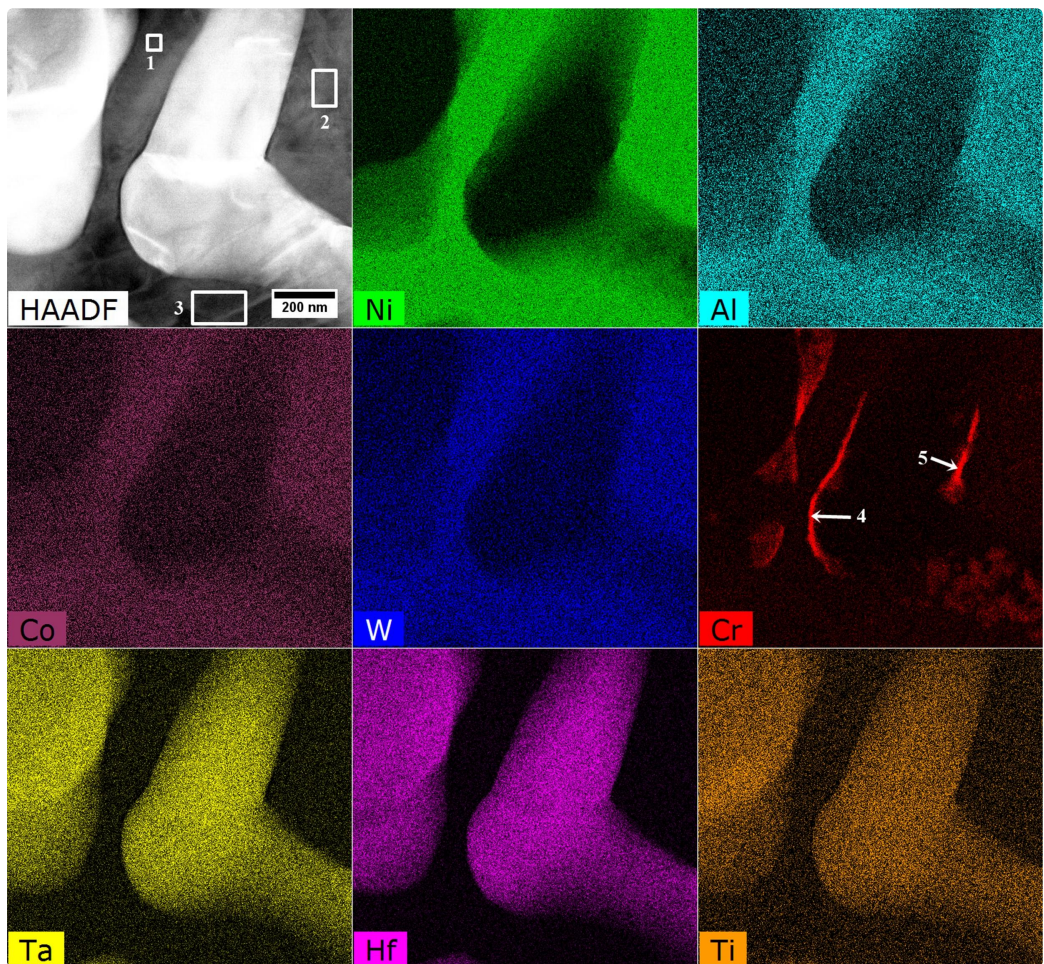**Figure 17. Microstructure of "chinese script" carbide in interdendritic space, STEM-HAADF**

Figure 18. Distribution of selected alloying element in the fragment of "chinese script" carbide, STEM-EDX

Table 4. Chemical composition of the coarse secondary γ' and M$_{23}$C$_6$ (at the MC carbide edge), at%

Area	Phase	Cr	Co	W	Al	Hf	Ta	Ti	Mo	Ni
1		3.0	7.5	3.3	11.8	1.1	2.7	1.7	0.5	68.4
2	Coarse secondary γ'	3.5	7.3	2.7	10.9	1.0	2.6	1.8	0.8	69.6
3		3.4	7.3	2.9	11.5	0.9	2.7	1.8	0.6	68.8

4	43.7	4.5	2.0	6.2	3.3	6.5	2.7	1.9	29.4
$M_{23}C_6$									
5	53.3	6.3	4.0	2.5	2.8	5.3	1.6	2.2	22.0

Locally on the edges of MC carbides, nano-layers with width 5-15 nm are present (Figure 19a-b). Reflections assigned to the FFT image correspond to the $M_{23}C_6$ carbide, which possesses a cubic crystal structure composed of 116 atoms ($D8_4$ type). In order to reveal the distribution of selected elements at the $M_{23}C_6$/γ' and $M_{23}C_6$/MC interfaces, additional linear measurements were performed (Figure 19c). The Cr smooth distribution changes at the interfaces γ'/$M_{23}C_6$ and $M_{23}C_6$/MC, indicating that the presence of $M_{23}C_6$ carbides can be explained by the interaction between the MC carbide and the matrix during the heat treatment.
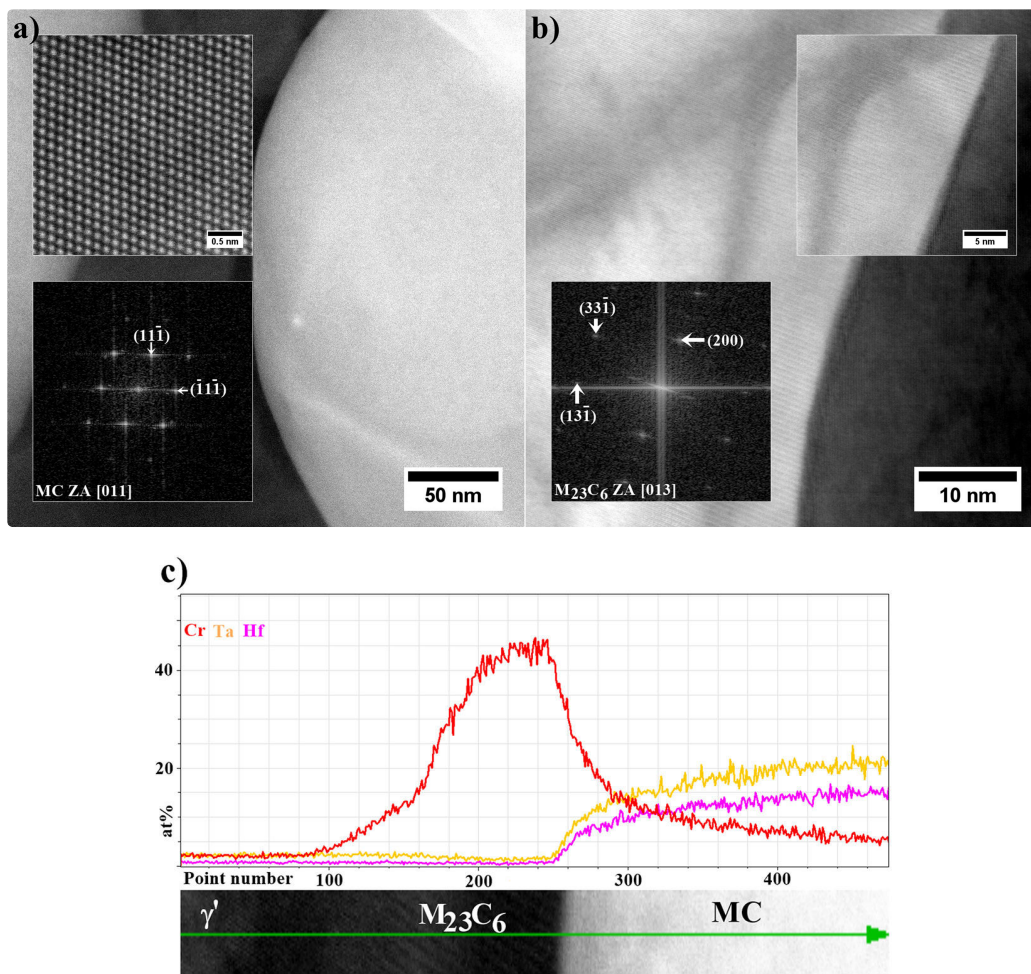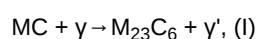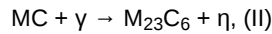

Figure 19. a) atomic structure and FFT image of MC carbide (STEM-HAADF); b) the nano-precipitate of $M_{23}C_6$ at the MC edge (STEM-BF); c) linear distribution of Cr, Hf and Ta (STEM-EDX)

$M_{23}C_6$ carbides are formed in medium- and high-chromium superalloys during casting's crystallization, heat treatment or annealing in the range of 760-980 ˚C. The alloying elements replacing chromium in the crystal lattice could increase the lattice parameter [8]. The position of M is mainly occupied by Cr. However, numerous alloying elements, including Mo and W, lead to a much more complex composition, e.g. $Cr_{21}(Mo, W)_2C_6$ and $(Ni, Co, Fe, Cr)_{21}(Mo, W)_2C_6$. In superalloys with increased iron content, it can be expected that they will partially replace chromium. In the solid-state, the $M_{23}C_6$ carbides are precipitating directly from the carbon-enriched γ matrix or by the decomposition reaction of the MC carbide, usually along grain boundaries, at twin boundaries, and on stacking faults [38][39]. Long-term service or heat treatment of superalloys at elevated temperatures may lead to the decomposition of MC carbides into more stable $M_{23}C_6$ and M_6C with lower carbon content, according to the following reactions [23]:

$$MC + γ \rightarrow M_{23}C_6 + γ', \text{ (I)}$$

$$MC + \gamma \rightarrow M_{23}C_6 + \eta, \text{ (II)}$$

$$MC + \gamma \rightarrow M_6C + \gamma', \text{ (III)}$$

The similarity in crystal structure sometimes makes the M_6C and $M_{23}C_6$ carbides challenging to distinguish. The M_6C usually replace $M_{23}C_6$ carbides in alloys containing approximately over 6 wt% Mo plus its atomic equivalent in W (weight per cent Mo plus one half the weight per cent W) [9][40][41]. The combined HRSTEM and STEM-EDX analyses show that I-type phase transformation occurred in René 108 during heat-treatment. The same transformation was also observed in crept Inconel 713C superalloy at 982 °C [42][43]. The Cr-rich $M_{23}C_6$ carbides were then precipitated along the grain boundaries in the form of blocks surrounded by the γ' precipitates. The degradation of the microstructure after annealing of the GTD111 superalloy at lower temperatures, 927 °C and 871 °C, mainly included the type II transformation [44]. The η phase (tetragonal structure with a=b=5.09 Å, c=8.29 Å) was particularly favoured by the enrichment of MC carbides in Ti and Ta because the Ti/Al concentration ratio in the superalloy exceeded 1.5. Relatively high Ti/Al ratio in superalloys promotes η phase formation, which, due to significant difference in lattice parameter compared to γ matrix, sensitizes the η/γ interface to crack nucleation and consequently decreases creep rupture life [45][46][47]. In this study, the Ti/Al relationship is 0.125, which is not favourable for the II-type phase transformation. The last possible phase transformation includes the formation of M_6C. The nano M_6C carbides discontinuously precipitated in the γ matrix or along γ/γ' interfaces of the crept K416B superalloy (1100 °C) were found by Xie [48]. Based on the thermodynamic analyses, solubility of C in the γ phase decreases during creep, which leads to its segregation in the stress concentration areas and then combining with carbide-formers as W.

During the SEM observation, precipitates with a clear and bright contrast (high Z-number) are revealed along the grain boundaries. This area has also been subjected to detailed STEM and HRSTEM studies. Figure 20 shows the microstructure of the precipitates along the grain boundary and the distribution of Ni, W and Cr in this area. The morphology and size of these precipitates are the same as these at the γ/γ' interfaces. The second similarity is enrichment in the same alloying elements. Their nanostructure with the corresponding FFT image is presented in Figure 21. The M_5B_3 borides are confirmed. Imaging of these phase using tilting of grain boundary region allow revealing a lot of precipitates. On the SEM-BSE such precipitates agglomeration is shown as a continuous or semi-continuous layer.
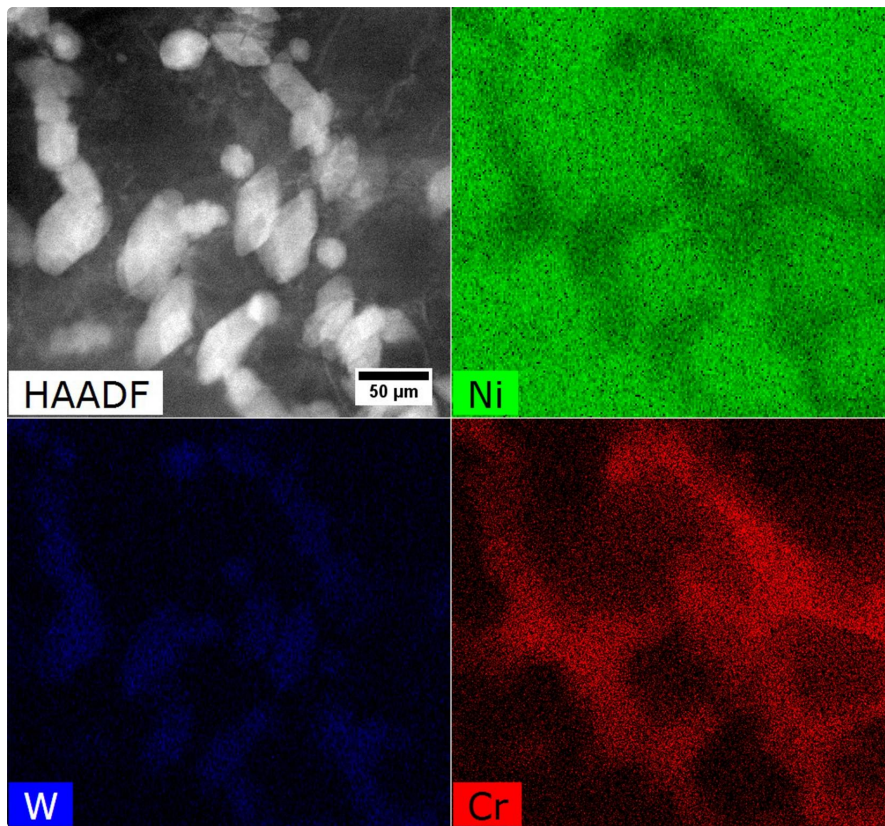

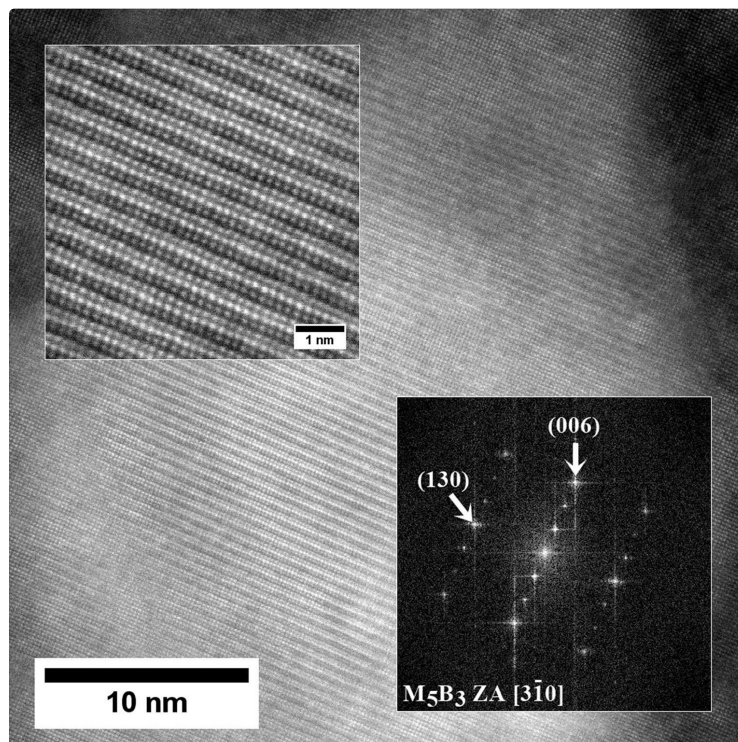**Figure 20. Distribution of selected alloying elements at the grain boundary, STEM-EDX**

Figure 21. Nanostructure of the M_5B_3 boride located at grain boundary, HRSTEM-HAADF

It has been shown that the addition of boron to Ni-based superalloys could significantly influence the grain boundary precipitation [31][49][50]. B atoms are larger than those of the other interstitial atoms and smaller than those of the substitutional atoms in Ni-based superalloys. So the lattice distortion caused by boron is considerable. The small diameter of boron allows it to fill vacancies at the grain boundaries, reducing the diffusivity in these regions [51]. During the ageing-treatment, boron segregation to the grain boundaries occurs and a large number of solute atoms, such as tungsten, chromium, and molybdenum, distribute at the grain boundaries. Because W, Cr, and Mo are more inclined to dissolve in the γ matrix when intermetallic γ′ phase is formed, these elements would be expelled and gather at the γ/γ′ interfaces. As a result, B would interact with W, Cr, and Mo and form M_5B_3 borides. Their formation at the grain boundary would pin the grain boundary and impede the grain-boundary sliding mechanism at high-temperatures. Xiao [52] suggested that any strong interaction between B atoms and dislocation cores could hinder dislocation motion and thus increase resistance to fatigue failure.

Acknowledgements

References

1. Reed, R.C. The Superalloys: Fundamentals and Applications, Cambridge University Press: Cambridge, UK, 2006.

2. Grudzień-Rakoczy, M.; Rakoczy, Ł.; Cygan, R.; Kromka, F.; Pirowski, Z.; Milkovič, O. Fabrication and characterization of the newly developed superalloys based on Inconel 740. Materials 2020, 13, 2362. https://dx.doi.org/10.3390%2Fma13102362

3. Rogalski, G.; Świerczyńska, A.; Landowski, M.; Fydrych, D. Mechanical and microstructural characterization of TIG welded dissimilar joints between 304L austenitic stainless steel and Incoloy 800HT nickel alloy. Metals 2020, 10, 559. https://doi.org/10.3390/met10050559

4. Rakoczy, Ł.; Cempura, G.; Kruk, A.; Czyrska-Filemonowicz, A.; Zielińska-Lipiec, A. Evolution of γ′ morphology and γ/γ′ lattice parameter misfit in a nickel-based superalloy during non-equilibrium cooling. Int. J. Mater. Res. 2019, 110, 66–69. DOI 10.3139/146.111729.

5. Sims, C.T. A History of Superalloy Metallurgy for Superalloy Metallurgists, Proceedings of the Fifth International Symposium on Superalloys, Pittsburgh, PA, USA, 7-11 October 1984; pp. 399-419. https://doi.org/10.7449/1984%2FSuperalloys_1984_399_419

6. Reed, R. C.; Rae, C. M. F. 22—Physical Metallurgy of the Nickel-Based Superalloys. In Physical Metallurgy, 5th ed.; Laughlin, D. E., Hono, K., Eds.; Elsevier: Oxford, UK, 2014; pp. 2215–2290, ISBN 978-0-444-53770-6.

7. Satyanarayana D., Prasad NE. Nickel-based superalloys technologies. In Aerospace Materials and Material Technologies, Eswara Prasad, N., Wanhill, R. J. H., Eds.; Springer: Singapore, 2017; pp. 199-228. https://doi.org/10.1007/978-981-10-2134-3

8. Kishawy H.A., Hosseini A. Superalloys. In Machining Difficult-to-Cut Materials. Basic Principles and Challanges. Springer, Cham, Switzerland, 2019. https://doi.org/10.1007/978-3-319-95966-5_4

9. Sabol, G. P.; Stickler, R. Microstructure of Nickel-Based Superalloys. Phys. Stat. Sol. 1969, 35 (11), 11-52. https://doi.org/10.1002/pssb.19690350102

10. Geddes, B.; Leon, H.; Huang, X. Superalloys: Alloying and Performance. ASM International, 2010. ISBN: 978-1-61503-040-8

11. Bradley, A. J.; Taylor, A. An X-ray analysis of the nickel–aluminium system. Proc. R. Soc. London Ser. A Math. Phys. Sci. 1937, 159, 56–72

12. Calmon, J. From Sir Frank Whittle to the year 2000 - what is new in propulsion? Aeronaut Astronaut, 1988, 6, 32-46. https://doi.org/10.1017/S0001924000016535

13. Ennis, P. 6- Nickel-Base Alloys for Advanced Power Plant Components. In Coal Power Plant Materials and Life Assessment, Shimbli, A. Eds; Woodhead Publishing: Shaston/Cambridge, UK, 2014; pp. 147–167. https://doi.org/10.1533/9780857097323.1.147

14. White, C.H. Nickel base alloys. In The development of gas turbine materials, 1st Ed; Meetham, G. W. Eds; Springer: Dordrecht, Netherlands, 1981; 89-119 https://doi.org/10.1007/978-94-009-8111-9

15. Rakoczy, Ł.; Cygan, R.; Analysis of temperature distribution in shell mould during thin-wall superalloy casting and its effect on the resultant microstructure. Arch. Civ. Mech. Eng. 2018, 18, 144-1450. https://doi.org/10.1016/j.acme.2018.05.008

16. Rakoczy, Ł.; Grudzień, M.; Cygan, R. Zielińska-Lipiec, A. Effect of cobalt aluminate content and pouring temperature on macrostructure, tensile strength and creep rupture of Inconel 713 castings. Arch. Metall. Mater. 2019, 63 (3), 1537-1545. http://dx.doi.org/10.24425/123845

17. Eiselstein, H.L. Metallurgy of a columbium-hardened nickel-chromium-iron alloy. In Advances in the Technology of Stainless Steels and Related Alloys, ASTM STP 369: West Conshohocken, PA, USA, 1965; 62–77. https://doi.org/10.1520/STP369-EB

18. Smith, S.R.; Carter, W.J.; Mateescu, G.D.; Kohl, F.J.; Fryburg, G.C.; Stearns, C.A. ESCA study of oxidation and hot corrosion of nickel-base superalloys. Oxid Met. 1980, 14, 415–435. https://doi.org/10.1007/BF00603610

19. Wilson, A.S. Formation and effect of topologically close-packed phases in nickel-base superalloys. Mat. Sci. and Tech. 2017, 33 (9), 1108-1118. https://doi.org/10.1080/02670836.2016.1187335

20. Morinaga, M.; Yukawa, N.; Adachi, H.; Ezaki, H. New phacomp and its applications to alloy design, In Proceedings of the Fifth International Symposium on Superalloys, Pittsburgh, PA, USA, 7-11 October 1984; pp. 523-532

21. Muktinutalapati, R.N. Materials for Gas Turbines – An Overview, In Advances in Gas Turbine Technology, Ed. Ernesto Benini, Eds; IntechOpen: Rijeka, Croatia, 2011, pp. 293-314. DOI: 10.5772/20730. https://www.intechopen.com/books/advances-in-gas-turbine-technology/materials-for-gas-turbines-an-overview

22. Rakoczy, Ł.; Milkovič, O.; Rutkowski, B.; Cygan, R.; Grudzień-Rakoczy, M.; Kromka, F.; Zielińska-Lipiec, A. Characterization of γ′ Precipitates in Cast Ni-Based Superalloy and Their Behaviour at High-Homologous Temperatures Studied by TEM and in Situ XRD. Materials 2020, 13, 2397.

23. Donachie, M.J.; Donachie, S.J. Superalloys: A Technical Guide, 2nd Ed.; ASM International: Materials Park, OH, USA, 2002.

24. Burt, H.; Dennison, J.P.; Elliot, I.C.; Wilshire, B. The effect of hot isostatic pressing on the creep and fracture behaviour of the cast superalloy Mar 002. Mat. Sci. Eng. 1982, 53 (2), 245-250. https://doi.org/10.1016/0025-5416(82)90057-X

25. Maslenkov, S.B.; Burova, N.N.; Khangulov, V.V. Effect of hafnium on the structure and properties of nickel alloys. Met. Sci. Heat Treat. 1980, 22, 283-285. https://doi.org/10.1007/BF00779883

26. Dahl, J.M.; Danesi, W.F.; Dunn, R.G. The partitioning of refractory metal elements in hafnium-modified cast nickel-base superalloys. Metall. Mater. Trans B.1973, 4, 1641. https://doi.org/10.1007/BF02668022

27. da Silva Costa, A.M.; Nunes, C.A.; Baldan, R.; Coelho, G.C. Thermodynamic Evaluation of the Phase Stability and Microstructural Characterization of a Cast B1914 Superalloy. J. Mat. Eng. and Perform. 2014, 23, 819–825. https://doi.org/10.1007/s11665-013-0814-6

28. Maxwell, D.H.; Baldwin, J.F.; Radavich, J.F. New concept in superalloy ductility. Metall. and Metal Form. 1975, 42, 332.

29. Ouichou, L.; Lavaud, F.; Lesoult, G.; Influence of the chemical composition of nickel-base superalloys on their solidification behavior and foundry performance. In Proceedings Superalloys 1980 (Fourth International Symposium), Champion, The Seven Springs International Symposium Committee, Pennsylvania, US, 1980; 235-244

30. Rakoczy, Ł.; Grudzień-Rakoczy, M.; Cygan, R. The influence of shell mold composition on the as-cast macro- and micro-structure of thin-walled IN713C superalloy casting. J. Mat. Eng. Perform. 2019, 28 (7), 3974-3985. https://doi.org/10.1007/s11665-019-04098-9

31. Kontis, P.; Mohd Yusof, H.A.; Pedrazzini, S.; Danaie, M.; Moore, K.L.; Bagot, P.A.J.; Moody, M.P.; Grovenor, C.R.M.; Reed, R.C. On the effect of boron on grain boundary character in a new polycrystalline superalloy. Act. Mat. 2016, 103, 688-699. https://doi.org/10.1016/j.actamat.2015.10.006

32. Hu, X.; Zhu, Y.; Sheng, N.; Ma, X.L. The Wyckoff positional order and polyhedral intergrowth in the M3B2- and M5B3-type boride precipitated in the Ni-based superalloys. Sci Rep. 2014, 4, 7367. https://doi.org/10.1038/srep07367

33. Strunz, P.; Petrenec, M.; Polák, J.; Gasser, U.; Farkas, G. Formation and dissolution of γ' precipitates in IN792 superalloy at elevated temperatures. Metals 2016, 6, 37. https://doi.org/10.3390/met6020037

34. Jena, A.K.; Chaturvedi, M.C. The role of alloying elements in the design of nickel-base superalloys. J. Mat. Sci. 1984, 19, 3121–3139. https://doi.org/10.1007/BF00549796

35. Rakoczy, Ł.; Grudzień, M.; Zielińska-Lipiec, A. Contribution of microstructural constituents on hot cracking of MAR-M247 nickel based supealloy. Arch. Met. Mat. 2018, 63 (1), 181-189. http://dx.doi.org/10.24425/118926

36. Bertaut, F.; Blum, P. Etude des borures de chrome. Compt. Rend. Hebd. Seances Acad. Sci. 1953, 236, 1055-1056

37. Long, H.; Mao, S.; Liu, Y.; Zhang, Z.; Han, X. Microstructural and compositional design of Ni-based single crystalline superalloys. J. All. Comp. 2018, 743, 203–220. https://doi.org/10.1016/j.jallcom.2018.01.224.

38. Davis, J.R. Heat-Resistant Materials; ASM International: Materials Park, OH, USA, 1997.

39. K. Ducki. Microstructural aspects of deformation, precipitation and strengthening processes in austenitic Fe-Ni superalloy; Silesian University of Technology, Poland, 2010. (in Polish)

40. Grudzień, M.; Tuz, L.; Pańcikiewicz, K.; Zielińska-Lipiec, A. Microstructure and properties of a repair weld in a nickel based superalloy gas turbine component. Adv. Mater. Sci. 2017, 17, 55–63. https://doi.org/10.1515/adms-2017-0011

41. Hanning, F.; Khan, A.K.; Steffenburg-Nordenström, J.; Ojo, O.; Andersson, J. Investigation of the Effect of Short Exposure in the Temperature Range of 750–950°C on the Ductility of Haynes® 282® by Advanced Microstructural Characterization. Metals 2019, 9 (12), 1357. https://doi.org/10.3390/met9121357

42. Rakoczy, Ł.; Grudzień, M.; Cygan, R. Influence of melt-pouring temperature and composition of primary coating of shell mold on tensile strength and creep resistance of Ni-based superalloy. J. Mat. Eng. Perform. 2019, 28, 3826-3834. https://doi.org/10.1007/s11665-018-3853-1

43. Grudzień, M.; Cygan, R.; Pirowski, Z.; Rakoczy, Ł.; Microstructural characterization of Inconel 713C superalloy after creep testing. Trans. Found. Res. Inst. 2018, 58 (1), 39-45. https://dx.doi.org/10.7356/iod.2018.04

44. Choi, B.G.; Kin, I.S.; Kim, D.H.; Seo, S.M.; Jo, C.Y. Eta phase formation during thermal exposure and its effect on mechanical properties in Ni-base superalloy GTD 111. In Proceedings of the 10th International Symposium Superalloys, Pittsburgh, PA, USA, 19–23 September 1996; pp. 163–172

45. Long, H.; Mao, S.; Liu, Y.; Zhang, Z.; Han, X. Microstructural and compositional design of Ni-based single crystalline superalloys. J. All. Comp. 2018, 743, 203–220. https://doi.org/10.1016/j.jallcom.2018.01.224

46. Nunomura, Y.; Kaneno, Y.; Tsuda, H.; Takasugi, T. Phase relation and microstructure in multi-phase intermetallic alloys based on Ni3Al-Ni3Ti-Ni3V pseudo-ternary alloy system. Intermetall. 2004, 12 (4), 389-399. https://doi.org/10.1016/j.intermet.2003.12.011

47. Xu, Y.; Yang, C.; Xiao, X.; Cao, X.; Jia, G.; Shen, Z. Evolution of microstructure and mechanical properties of Ti modified superalloy Nimonic 80A. Mat. Sci. Eng. A. 2001, 530 (15), 315-326. https://doi.org/10.1016/j.msea.2011.09.091

48. Xie, J.; Yu, J.; Sun, X.; Jin, T. Thermodynamics analysis and precipitation behavior of fine carbide in K416B Ni-based superalloy with high W content during creep. Trans. Nonferrous Met. Soc. China. 2015, 25, 1478-1483. https://doi.org/10.1016/S1003-6326(15)63748-7

49. Li, Q.; Lin, X.; Wang, X.; Yang, H.; Song, M.; Huang, W. Research on the Grain Boundary Liquation Mechanism in Heat Affected Zones of Laser Forming Repaired K465 Nickel-Based Superalloy. Metals 2016, 6, 64. https://doi.org/10.3390/met6030064

50. Kang, B.; Han, C.; Shin, Y.; Youn, J.; Kim, Y. Effects of boron and zirconium on grain boundary morphology and creep resistance in Nickel-based superalloy. J. of Mat. Eng and Perform. 2019, 28, 7025–7035. https://doi.org/10.1007/s11665

-019-04419-y

51. Tytko, D.; Choi, P.P.; Klöwer, J.; Kostka, A.; Inden, G.; Raabe, D. Microstructural evolution of a Ni-based superalloy (617B) at 700°C studied by electron microscopy and atom probe tomography. Acta Mater. 2012, 60, 1731-1740. https://doi.org/10.1016/j.actamat.2011.11.020

52. Xiao, L.; Chen, D.L.; Chaturvedi, M.C. Effect of boron on fatigue crack growth behavior in superalloy IN718 at RT and 650°C. Mater. Sci. Eng. A 2006, 428,1-2, 1–11. https://doi.org/10.1016/j.msea.2005.08.206